Retrieval of aerosol optical properties from GOCI-II observations: Continuation of long-term geostationary aerosol monitoring over East Asia

Seoyoung Lee[1,a], Myungje Choi[2,3], Jhoon Kim[1,*], Young-Je Park[4], Jongkuk Choi[4], Hyunkwang Lim[5], Jeewoo Lee[1], Minseok Kim[1], Yeseul Cho[1]

[1]Department of Atmospheric Sciences, Yonsei University, Seoul, Republic of Korea

[2]University of Maryland, Baltimore County, Baltimore, MD, USA

[3]NASA Goddard Space Flight Center, Greenbelt, MD, USA

[4]Korea Ocean Satellite Center, Korea Institute of Ocean Science and Technology, Busan, Republic of Korea

[5]National Institute for Environmental Studies, Tsukuba, Japan

[*] Corresponding to: J. Kim (jkim2@yonsei.ac.kr)

[a] Present address: University of Maryland, Baltimore County, Baltimore, MD, USA and NASA Goddard Space Flight Center, Greenbelt, MD, USA

Keywords: aerosol, geostationary satellite, AOD, GOCI, GOCI-II

Abstract

Since the Geostationary Ocean Color Imager (GOCI) was successfully launched in 2010, the GOCI Yonsei aerosol retrieval (YAER) algorithm has been continuously updated to retrieve hourly aerosol optical properties. GOCI-II has 4 more channels including UV, finer spatial resolution (250 m), and daily full disk coverage as compared to GOCI, and was launched in February 2020, onboard the GEO-KOMPSAT-2B (GK-2B) satellite. In this study, we extended the YAER algorithm to GOCI-II data based on its improved performance in many aspects and present the first results of aerosol optical properties retrieved from GOCI-II data. Utilizing the overlapping period between the GOCI-II and GOCI in geostationary Earth orbit, we present GOCI-II aerosol retrievals for high aerosol-loading cases over East Asia and show that these have a consistent spatial distribution with those from GOCI. Furthermore, GOCI-II provides AOD at an even higher spatial resolution, revealing finer changes in aerosol concentrations. Validation results for one year data show that the GOCI-II AOD has a correlation coefficient of 0.83 and a ratio within the expected error (EE) of 59.4% when compared with the aerosol robotic network (AERONET) data. We compared statistical metrics for the GOCI and GOCI-II AODs to assess the consistency between the two datasets. In addition, it was found that there is a strong correlation between the two datasets from the comparison of gridded GOCI and GOCI-II AOD products. It is expected that data from GOCI-II will continue long-term aerosol records with high accuracy that can be used to address air-quality issues over East Asia.

1. Introduction

Atmospheric aerosols play a crucial role in Earth's climate system by directly absorbing and scattering sunlight and indirectly changing the microphysics of clouds (Li et al., 2022). The impact of aerosols on air quality has become a serious issue, as they degrade visibility and are detrimental to human health, causing cardiovascular and respiratory diseases (Hyslop, 2009; WHO, 2016). The effects of atmospheric aerosols on the climate system and human health are difficult to quantify because of their short lifetimes, irregular distribution in terms of time and space, and their complex physical and chemical characteristics. To better understand the impact of aerosols on air quality and on the climate system, the demand for continuous and accurate aerosol observation records is increasing.

Among the various types of observation used for analysis and monitoring of atmospheric aerosols, satellite observations have the advantage of covering a wider area than airborne and ground-based instrumentations. Therefore, comprehensive analysis of aerosol characteristics and trends using satellite observations have been widely reported (Eom et al., 2022; Jin et al., 2023). However, generating long-term aerosol data sets from space-borne observations is challenging due to the limited lifetime and different calibration status of satellite sensors. To achieve long-term aerosol optical depth (AOD) datasets from satellite observations, several studies have applied the same aerosol retrieval algorithm to data from different instruments. For example, Levy et al. (2015) generated a long-term AOD database by using the dark target (DT) algorithm for data from Moderate Resolution Imaging Spectroradiometers (MODIS) onboard the Terra and Aqua platform and from the Visible Infrared Imaging Radiometer Suite (VIIRS). Subsequently, Sawyer et al. (2020) conducted an analysis to assess the spatial and temporal variations between these datasets, ensuring their consistency. With a similar objective, Sayer et al. (2019) validated the deep blue (DB) aerosol products derived from MODIS and VIIRS and also verified their consistency. These studies confirm that it is

beneficial to apply the same aerosol retrieval techniques to data acquired from different platforms to generate consistent, long-term aerosol data records.

The Geostationary Ocean Color Imager (GOCI) onboard the Communication, Ocean, and Meteorology Satellite (COMS) is the first multi-channel (six visible and two near-infrared) ocean color sensor in geostationary Earth orbit (GEO; Choi et al., 2012). Since its successfully launched in 2010, GOCI data has been utilized in various studies with several methods such as look-up table (LUT) based approaches and machine learning techniques for the retrieval of aerosol optical properties (Kang et al., 2022; Zhang et al., 2014).

The Yonsei aerosol retrieval (YAER) algorithm has been developed to retrieve hourly aerosol optical properties using GOCI at a spatial resolution of 6 km (Choi et al., 2016, 2018; Lee et al., 2010a). These aerosol optical properties include AOD, fine-mode fraction (FMF), single-scattering albedo (SSA) and Ångström exponent (AE). Choi et al. (2019) reported that the accuracy of GOCI YAER version 2 (V2) products is comparable to that of other satellite-based products when compared with ground-based measurements. The GOCI YAER product has been used in many studies to analyze air quality in East Asia because of its high spatiotemporal resolution and its accuracy with respect to ground observations (Zhai et al., 2021; Park et al., 2014, 2019; Pendergrass et al., 2022; Lee et al., 2019, 2021; Koo et al., 2020). The operation of GOCI was terminated in March 2021, accumulating 10 years of GOCI YAER data record, to provide a unique long-term hourly-scale aerosol property record in East Asia.

To continue the mission, GOCI-II, the second generation of GOCI, was launched onboard GEO-KOMPSAT-2B (GK-2B) in February 2020, further improving GOCI's capability to continuously monitor marine and atmospheric environments (Choi et al., 2021). GOCI-II has advanced functional, radiometric, and geometric performances compared to GOCI (Ahn et al.,

2010; Coste et al., 2016). GOCI-II now has a UV channel at 380 nm and three additional bands in visible (VIS) and near-infrared (NIR) regions and doubled the spatial resolution to ~250 m at nadir. To take advantage of these advances of GOCI-II, it is highly desirable to investigate the feasibility of extending the GOCI YAER algorithm to GOCI-II.

In this study, we applied the YAER algorithm to GOCI-II observations to generate a high-accuracy long-term aerosol dataset over East Asia, and validated against the AERONET for one year and GOCI for the overlapping period in GEO. The characteristics of the GOCI-II instruments and the YAER algorithm are presented in Section 2. Section 3 presents the first GOCI-II YAER AOD results and compares these with ground-based AOD observations over East Asia. The consistency between the AODs retrieved from GOCI and GOCI-II is discussed in Section 4. The overlapping time series of the retrievals from the two sensors are also shown in Section 4, and we present our conclusions in Section 5.

2. Data and Methods

2.1. GOCI-II instrument

GOCI-II, the second generation of GOCI, is still a unique ocean color sensor in GEO, which was launched on February 19, 2020. After completing its initial in orbit tests (IOT), GOCI-II has been in regular operation since October 2020 with the goal of operating for ten years. Table S1 compares the characteristics of GOCI and GOCI-II. GOCI-II has improved functional, radiometric, and geometric capabilities compared to GOCI. Ground-sampling distance (GSD) has been improved from 500 to 250 m, and the field of regard has been extended to cover the whole Earth disk. For local-area imaging, GOCI-II covers 2,500 km × 2,500 km around the Korean Peninsula, which is similar to the area covered by GOCI (Fig. S1). GOCI-II acquires local area images with 12 slots 10 times per day and full-disk image

once a day during daytime. Each slot is imaged at 12 GOCI-II channels including UV, VIS, and NIR bands between 380 and 865 nm. The spectral response functions for GOCI and GOCI-II are shown in Fig. S2. GOCI-II has four additional channels centered at 380, 520, 620, and 709 nm, in addition to the existing eight channels for GOCI. GOCI-II also has a wideband channel, which is designed for star imaging to improve image navigation and registration (INR) processing.

After launch, it was confirmed that all GOCI-II functions operated normally during the Initial Activation Checkout (IAC) stage. Also, performance and operation tests, radiometric calibration, and image geometry correction were conducted during the IOT stage (Yong et al., 2021). Subsequent radiometric calibration has been carried out periodically to monitor the temporal change in radiometric gain. However, starting from 20:00 UTC on January 4, 2021, the L1B data have been provided with on-ground radiometric gain parameters, leading GOCI-II radiances to have similar values to those obtained from GOCI. The ratios of on-ground to in-orbit radiometric gain parameters for the GOCI-II spectral bands, in order of increasing wavelength, are as follows: 0.9627, 0.95056, 0.95071, 0.95801, 0.93841, 0.98011, 0.9783, 0.96874, 0.95262, 0.92685, 0.91338, 0.88323, 0.962, and 0.95262, respectively. In this study, we implemented the aerosol retrieval algorithm with on-ground gain parameters by applying these ratios for GOCI-II observation data that were acquired before January 5, 2021.

2.2. GOCI-II Yonsei aerosol retrieval (YAER) algorithm

The GOCI-II YAER algorithm was developed based on the GOCI YAER algorithm, with adjustments to consider the new capabilities of GOCI-II. Figure S3 presents the GOCI-II YAER algorithm as a flowchart, and Table 1 summarizes the main differences between the GOCI YAER V2 and GOCI-II YAER algorithms. The first step in the GOCI-II YAER

algorithm is to eliminate pixels that are not valid for aerosol retrieval, such as those contaminated by clouds, snow, and/or bright surfaces. After removing invalid pixels, the remaining pixels are aggregated to pixels with a spatial resolution of 2.5 km for the AOD retrieval. The GOCI-II local area measurements consist of 12 slots, in which each slot has 2780 × 2780 pixels. The aggregated pixels have a spatial resolution of 2.5 km by aggregating 10 × 10 pixels, and a slot image is converted to an image of 278 × 278 pixels. The cloud-masking for GOCI-II combines the process used for the GOCI YAER V2 algorithm with the method based on the normalized difference vegetation index (NDVI) over ocean, as suggested by Ishida et al. (2011). Although these cloud detection methods share the same physical principles, the threshold values used to differentiate between cloudy and cloud-free pixels vary depending on the applied satellite instrument. Therefore, some of the threshold values for the GOCI-II cloud mask were optimized specifically for GOCI-II observations (Table S2).

Table 1. Major differences between the GOCI YAER V2 and GOCI-II YAER algorithms

Algorithm	GOCI YAER V2	GOCI-II YAER
Satellite data	GOCI L1B radiance	GOCI-II L1B radiance
Sample period for estimating land surface reflectance	5-year (March 2011-February 2016)	1-year (October 2020-November 2021)
Climatological wind speed data	ECMWF Interim (average for March 2011–February 2016)	ECMWF ERA5 (average for 2016–2020)
Channel selection for inversion procedure	(Land) GOCI spectral bands with surface reflectance less than 0.15 (Ocean) 412, 443, 745, 865 nm (Turbid water) 412, 865 nm	(Land) GOCI-II spectral band with surface reflectance less than 0.15 (Ocean) 380, 412, 443, 710, 745, 865 nm (Turbid water) 380, 412, 745, 865 nm
Number of aerosol models	26	6
Radiative transfer model	libRadtran	VLIDORT version 2.7
Spatial resolution of final aerosol products	6 km	2.5 km
Reference	Choi et al. (2018)	This study

In the next step, each pixel is classified as land, ocean, or turbid water. Surface reflectance values over land and turbid water are calculated for each month, channel, and hour using the minimum reflectivity technique (Hsu et al., 2004; Fukuda et al., 2013). The GOCI YAER V2 algorithm employed climatological land surface reflectance values calculated from five-year

GOCI data. Sufficient GOCI-II data to generate a surface reflectance climatology are not yet available, so we used the Lambertian Equivalent Reflectance (LER) for a month. The first and second minimum LER for each channel and hour were averaged for the surface reflectance. These values are considered to be the surface reflectance for the 15th day of each month, and we linearly interpolated from these to provide the required input to the GOCI-II YAER algorithm for each individual day. The ocean surface reflectance was obtained following the Cox and Munk method using a climatological wind speed database (Cox and Munk, 1954). The wind speed at ten meters above the surface was taken from the European Centre for Medium-Range Weather Forecasts (ECMWF) ERA5 dataset and averaged for each month during the five-year period from 2016 to 2020 (Copernicus Climate Change Service, 2017). In the same way as for the land surface reflectance, the averaged wind speed was taken as the value for the 15th day of each month and was linearly interpolated to each date.

Similar to the GOCI YAER algorithm, the GOCI-II YAER algorithm uses a pre-calculated LUT to reduce the time required to retrieve aerosol optical properties. Table S3 shows the LUT dimensions for the GOCI-II YAER algorithm. The top-of-atmosphere (TOA) reflectance is computed using the Vector Linearized Discrete Ordinate Radiative Transfer (VLIDORT) model version 2.7 (Spurr and Christi, 2019; Spurr, 2006), which considers wavelength, solar zenith angle, viewing zenith angle, relative azimuth angle, AOD, aerosol model, terrain height, and variables for surface reflectance. It is calculated by taking into account the spectral response function for each of the GOCI-II bands, as shown in Fig. S2. The node points used for the solar and satellite zenith angles are spaced at 10° intervals from 0° to 70°, and the relative azimuth angle is considered at 10° intervals from 0° to 180°.

The GOCI-II YAER algorithm uses Aerosol Robotic Network (AERONET) inversion data (Dubovik and King, 2000) to reflect the characteristics of aerosol models. AERONET version 2 Level 2 all-point inversion data are used for the period up to July 2017, and we selected global sites from which more than ten data records were available. While GOCI YAER algorithm used 26 aerosol models, 6 aerosol models were considered in GOCI-II YAER algorithm to reduce computational costs. This change resulted in the processing time being up to twice faster. We used the aerosol type classification method proposed by Lee et al. (2010b). The SSA at 440 nm and FMF at 550 nm from the AERONET data were used to classify six aerosol types: black carbon (highly-absorbing fine, moderately-absorbing fine, slightly-absorbing fine), non-absorbing fine, mixture, and dust. The aerosol optical properties (AOPs) are averaged for each aerosol model over three AOD ranges (0–0.5, 0.4–1.0, and 0.9–5.0 for AOD at 550 nm) to account for the fact that AOPs vary with AOD owing to hygroscopic growth effects or aggregation. In order to calculate the LUT, aerosol properties in the UV channel (<440 nm) are required. However, AERONET inversion data provides only for wavelength at 440, 670, 870, and 1020 nm. To address this, we extrapolated aerosol microphysical properties to the UV channel using the power-law for imaginary part of the refractive index (Saleh et al., 2014). The spectral dependences for black carbon, dust and non-absorbing fine aerosols are adopted the values suggested by Go et al. (2020), which estimated them using the Multifilter Rotating Shadowband Radiometer and AERONET observations at Yonsei University in Seoul. For mixture, we performed a linear extrapolation of aerosol microphysical properties into UV channel.

Since the GOCI-II YAER algorithm can only retrieve aerosol optical properties over dark surfaces, observation channels between 380 and 680 nm with a surface reflectance less than 0.15 were selected and used for our aerosol retrieval over land. We implemented the inversion calculations only when at least two channels met this criterion. To avoid the effect of the

water leaving radiance related to the optical properties of chlorophyll and colored dissolved organic matter, four channels were used over turbid water (centered at 380, 412, 745, and 865 nm), and six channels were used over the ocean (centered at 380, 412, 443, 710, 745, and 865 nm), similar to the GOCI YAER V2 algorithm (Choi et al., 2018).

We compared the pre-calculated LUT with the observed TOA reflectance and selected the aerosol models that minimized the standard deviation for the 550 nm AOD. We applied these models to the data from each channel to obtain the final AOD. The inversion method in the GOCI-II YAER algorithm is adopted from Choi et al. (2016) and Choi et al. (2018). The AOD at 550 nm was calculated for every wavelength and aerosol model using the LUT. If the selected aerosol type is correct, then the AODs calculated for all wavelengths should be identical when they are converted to 550 nm. Therefore, two aerosol models that minimize the standard deviation (σ) for the AODs at each wavelength were chosen. FMF, SSA, and AE were obtained from the σ-weighted average of the two selected models. The aerosol model was classified as one of the six aerosol types using the final retrieved FMF and SSA following the method suggested by Lee et al. (2010b).

3. Results and Discussions

3.1. First GOCI-II AOD retrieval and validation

Figure 1a shows the AOD at 550 nm around the Korean peninsula retrieved from GOCI-II observations on RGB image at 3:30 UTC on March 14, 2021. Aerosol optical properties including AOD at 550 nm, FMF at 550 nm, SSA at 440 nm, and AE between 440 and 870 nm for the field of regards of GOCI-II are depicted in Fig. S4, showing aerosol plume with high FMF (~0.93) and SSA (~0.96) over the Yellow Sea. AOD retrieved from GOCI-II show that the cloud masking in the YAER algorithm works well at a high spatial resolution as shown in

Fig. 1a. As with the GOCI image, some cloud-contaminated pixels remain in between and at cloud edges in the GOCI-II AOD image. Figure 1 shows that the GOCI-II and GOCI AOD results have similar magnitudes and spatial distributions. However, the GOCI-II AOD results include more detailed spatial information than the GOCI results because of their higher spatial resolution (2.5 km versus 6 km). The number of GOCI-II AOD retrievals is much greater than those of GOCI over land. It is noteworthy that there are more GOCI-II AOD retrievals at cloud-edges and between clouds, compared with the GOCI AOD retrievals, showing more detailed distribution of aerosols in the GOCI-II dataset. Overall, around five times as many AOD retrievals were calculated for GOCI-II (24,876) as compared to GOCI (5,504). Figure 1c is a histogram of the GOCI- and GOCI-II-retrieved AODs at 550 nm with bin size of 0.05 that are shown in Fig. 1a and 1b. When comparing histograms for the GOCI and GOCI-II AODs, the correlation coefficient between the numbers of data points in each AOD bin for GOCI and GOCI-II is 0.93, showing that the two AOD images have a similar distribution.

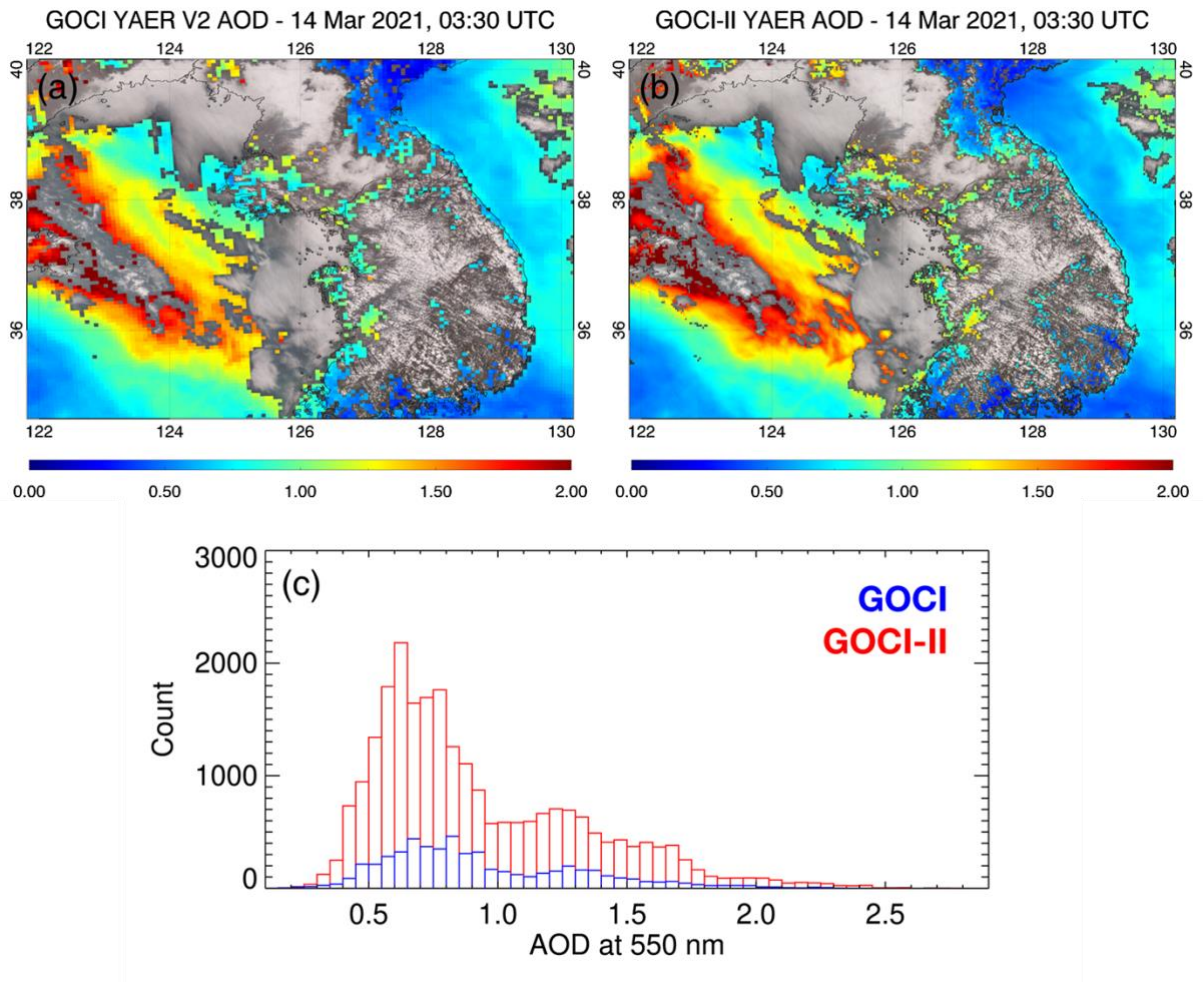

248

249 **Figure 1.** AOD at 550 nm retrieved using the YAER algorithm on March 14, 2021, at 03:30
250 UTC. (a) GOCI AOD at 6 km resolution and (b) GOCI-II AOD at 2.5 km resolution. (c)
251 Histograms of AOD at 550 nm for the GOCI (blue) and GOCI-II (red) data shown in (a) and
252 (b), respectively.

253

254 We compared GOCI-II AODs with co-located AERONET AODs for a year from November
255 2020 to October 2021 to investigate the accuracy of the GOCI-II YAER AOD. We used
256 AERONET version 3 Level 1.5 data from 43 stations because the Level 2.0 data for this
257 period had not yet been generated for most of the stations (Holben et al., 1998; Giles et al.,
258 2019). We averaged hourly data from GOCI-II AOD pixels within a 25 km radius of each
259 AERONET site and averaged AERONET data within 30 minutes of each GOCI-II

observation time. The averages from the datasets were used for the assessment when there was at least one measurement available from each dataset. The validation results over land and ocean are shown in Fig. 2. The statistical metrics for the evaluation are as follows: the number of collocation data (N), the Pearson's linear correlation coefficient (R), the root mean squared error (RMSE), the median bias error (MBE), and the fraction of data points within the expected error (EE) range. We used the EE range for the MODIS DT products [EE = ±(0.05 + 0.15 × AERONET AOD); Levy et al., 2007]. As shown in Fig. 2, the GOCI-II AOD has a correlation coefficient of 0.825 (0.810) and a ratio within the EE of 53.6% (72.9%) when compared with the AERONET data over land (ocean). There is an overestimation of GOCI-II AOD at low AERONET AODs which reflects the difficulty of removing clouds due to the lack of infra-red (IR) channels, similarly as in GOCI AOD retrievals. The land surface is more spatially inhomogeneous than the ocean, so the effect of cloud contamination is greater over land, and our validation results over land show relatively low accuracy compared with those over the ocean.

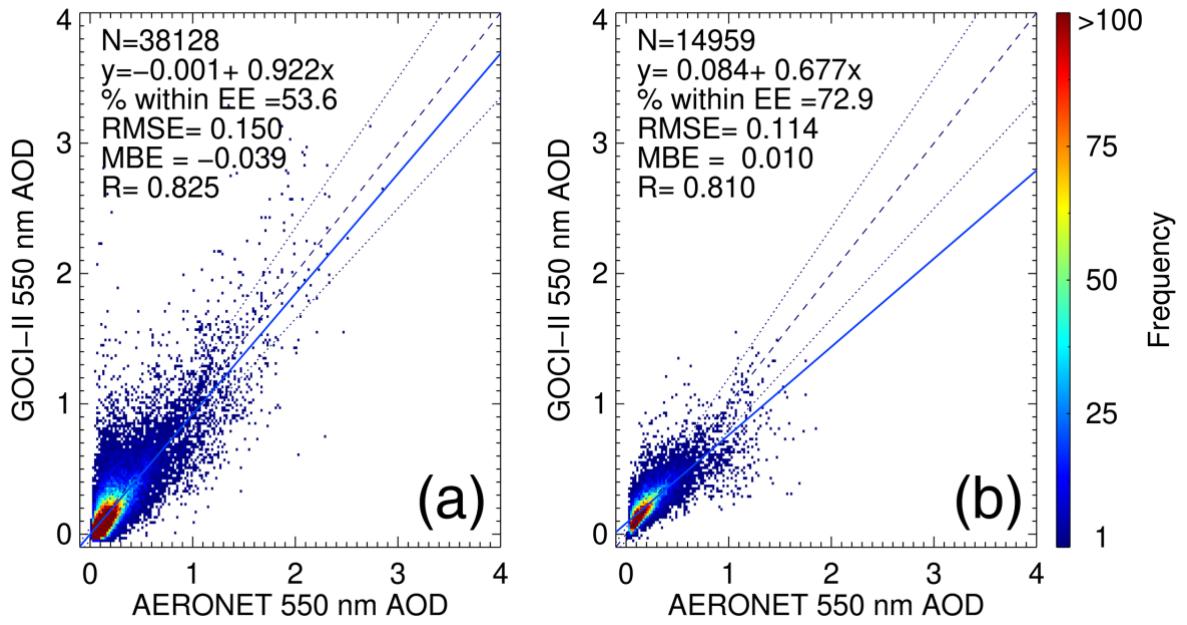

275

276 **Figure 2.** Comparison of 550 nm AOD from the GOCI-II YAER algorithm with AERONET
277 version 3 level 1.5 AOD over (a) land and (b) ocean surfaces during November 2020–October
278 2021. Black dashed lines represent the one-to-one line, and dotted lines represent the expected
279 error range from MODIS Dark Target AOD.

280

281 ## 3.2. Consistency between GOCI- and GOCI-II-retrieved AODs

282 GOCI observations are only available up to March 2021, the end of mission lifetime.
283 Therefore, this study attempted to investigate the possibility of continuing GOCI-derived
284 aerosol records beyond this date using long-term hourly aerosol data for East Asia derived
285 from GOCI-II. To ensure consistency between the GOCI and GOCI-II AODs, we compared
286 the results by their spatial distributions and by validation with ground-based observations. The
287 two satellite instrument data were compared for the 5-month overlapping operational period
288 from November 2020 to March 2021.

289 ### 3.2.1 Comparison of validation results

AERONET data were used as a reference to compare the accuracy of GOCI- and GOCI-II-retrieved AODs. Five months of AERONET version 3 Level 2.0 data from 31 sites were used (Fig. S1). Figure 3 shows a scatter plot for the GOCI and GOCI-II AODs against AERONET AOD. Comparing the number of data shows that the number of matched data for GOCI-II is larger than that for GOCI. This is because GOCI-II acquires ten observations per day from 08 KST (23 UTC) to 17 KST (08 UTC), whereas GOCI acquired eight observations per day.

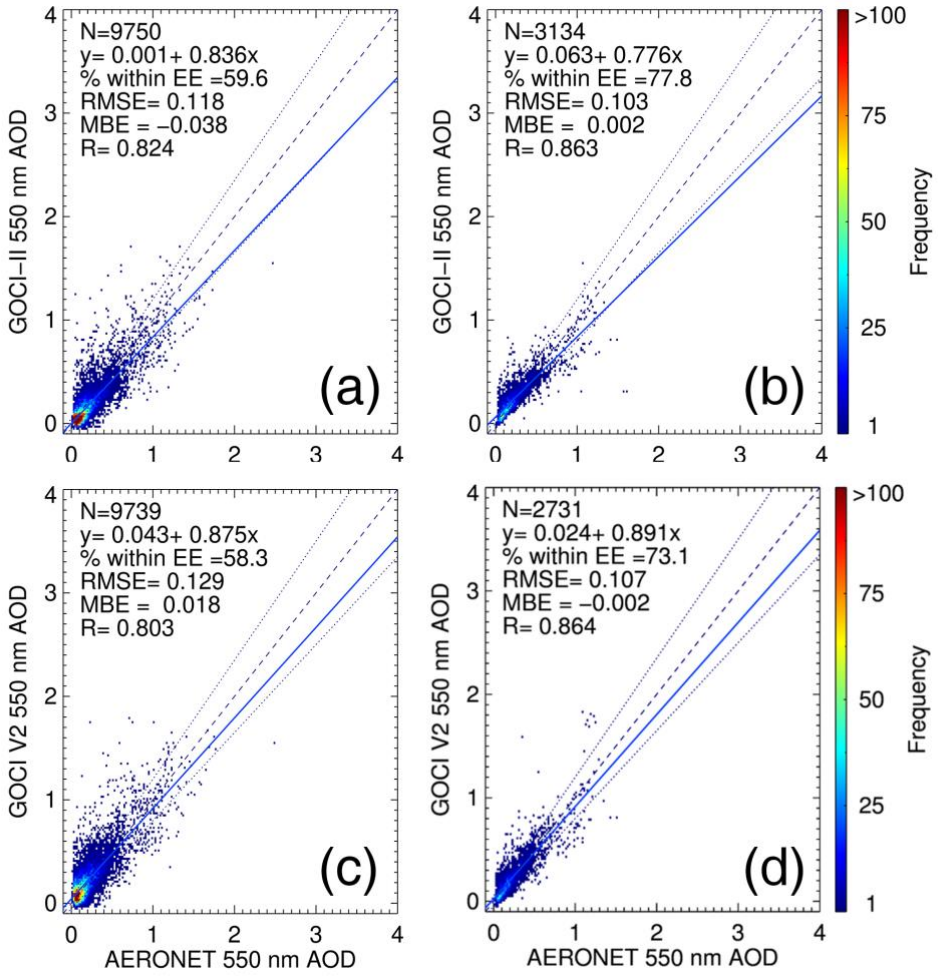

Figure 3. Comparison of AERONET version 3 level 2.0 AOD and (a) GOCI-II land AOD, (b) GOCI-II ocean AOD, (c) GOCI land AOD, and (d) GOCI ocean AOD during November 2020–March 2021. Black dashed lines represent one-to-one lines, and dotted lines represent the expected error ranges for MODIS Dark Target AOD.

The GOCI and GOCI-II AODs over land have high R-values of 0.803 and 0.824, respectively, when compared with the AERONET AOD. The RMSE for AOD over land is also similar for both datasets, 0.129 and 0.118 for GOCI and GOCI-II, respectively when compared with the AERONET. Both datasets include some overestimates due to cloud contamination. In future, these errors can be reduced by implementing improved cloud masking with IR channels on other meteorological sensors onboard the same satellite platform, such as Advanced Himawari Imager (AHI) or Advanced Meteorological Imager (AMI) (Choi et al., 2019). The fraction within the EE of GOCI-II is 59.6%, similar to that for GOCI (58.3%). The MBE for the GOCI-II AOD over land is −0.038, which is larger than and has the opposite sign from the MBE for GOCI, which is 0.018. This is inferred to reflect an error in the land surface reflectivity estimated for GOCI-II. Although both algorithms use the minimum reflectivity technique, GOCI uses climatological values calculated from a five-year dataset, whereas GOCI-II estimates surface reflectance using data from a single-year dataset. It is possible that surface reflectivity is over-estimated for GOCI-II compared with GOCI because it is relatively difficult to find dark pixels with cloud-free and aerosol-free conditions in a shorter-term dataset. It is possible that surface reflectivity is over-estimated for GOCI-II compared with GOCI because it is relatively difficult to find dark pixels with cloud-free and aerosol-free conditions in a shorter-term dataset. This overestimation of GOCI-II surface reflectance leads to underestimation of GOCI-II AOD shown in Figure 3. In future, as more GOCI-II data become available, improved land surface reflectivity estimates will become possible for GOCI-II. To demonstrate this, when surface reflectance is estimated using two-year data, the MBE for the GOCI-II AOD over land in Fig. 3a improved from −0.038 to −0.014 for the same period (Fig. S5). Furthermore, the increased spatial resolution of GOCI-II might contribute to larger errors in AOD retrieval. This could be attributed to the enhanced

complexities of surface reflectance, which may introduce additional uncertainties in the AOD retrieval.

We used data from coastal AERONET sites to validate AOD retrieved over the ocean. AOD retrieved over the ocean is more accurate than that retrieved over land for both satellite-derived datasets. The fractions within EE are greater than 70% for both the GOCI and GOCI-II AODs, and the RMSE for ocean AOD is low at 0.104 and 0.109 for GOCI and GOCI-II, respectively. Ocean AOD retrievals come from two surface reflectance conditions: one is over turbid water, and the other is over clear water. Although GOCI-II retrievals of AOD over turbid water used the surface reflectance estimate that was based on the minimum reflectance method with the short-term dataset, climatological wind speed was considered to estimate the ocean surface reflectivity. Therefore, since both methods are used, the validation of the GOCI-II AOD retrievals over the ocean does not show as much negative bias as over land. Overall, according to Figure 3, our validation of GOCI and GOCI-II-retrieved AODs shows comparable accuracies.

Validation of GOCI- and GOCI-II-retrieved AE, FMF, and SSA over ocean and land surfaces are presented in Fig. S6. The three variables were validated using AERONET version 3 level 2.0 inversion data for the same period as used for the AOD validation; i.e., November 2020 to March 2021. AE and FMF were compared when the AOD was above 0.3, and SSA was validated when the AOD was above 0.4. R-values for GOCI-II AE and FMF were approximately 0.6 and 0.7, respectively, when compared with the AERONET data, and the results for GOCI AE and FMF were similar, with R-values of approximately 0.4 and 0.5, respectively. To evaluate the accuracy of SSA, we used the ratios of GOCI and GOCI-II SSA to AERONET SSA for values in the ranges of ±0.03 and ±0.05. The ratio for GOCI-II SSA is similar to that for GOCI SSA. Although the accuracies of AE, FMF and SSA are high in GOCI-II, the dynamic ranges of retrieved parameters are narrower due to the reduced number

of aerosol models in GOCI-II YAER algorithm. In conclusion, our validation for AE, FMF, and SSA derived from GOCI-II data show that the retrievals show comparable accuracy to that found in our validation for GOCI-retrievals. However, note that the retrievals of AE, FMF, and SSA from the GOCI and GOCI-II YAER algorithms take predefined values for the selected aerosol model, resulting in lower accuracy for these retrievals than for AOD retrievals.

Next, we compared the validation statistics between the GOCI and GOCI-II AODs for each AERONET site. In Fig. 4, the x-axis represents the validation results for GOCI AODs, and the y-axis represents the validation results for GOCI-II AODs. The comparison used validation data from 31 AERONET stations, for which there were corresponding satellite-derived data from both GOCI and GOCI-II. The color of each point shows the average of the AERONET AOD at 550 nm in our validation. An almost identical number of data points were matched to each AERONET data point for GOCI and GOCI-II, although slightly more GOCI-II data were matched than GOCI data, as shown in Fig. 3. The RMSE, fractions within EE, MBE, and R-values were generally located on the one-to-one line, showing similar performance for the two AOD retrievals. Small differences in accuracy between the two satellite-derived AODs are assumed to be attributable to the instrument calibration and characteristics, the radiative transfer model, and the period of data used to estimate surface reflectances. As the averaged AERONET AOD increases, R increases and RMSE tends to decrease for both GOCI and GOCI-II. The fraction within EE for GOCI-II is high when the average AERONET AOD is low, and the GOCI AOD is more accurate by this measure than the GOCI-II AOD when the AERONET AOD is high. Areas with high average AOD tend to also have high background AOD, so the surface reflectance estimates used for the AOD-retrievals at those sites may be overestimated owing to the short-term nature of the dataset on which they are based. As shown in Fig 3, the MB is negative for the GOCI-II AOD at most AERONET sites due to

errors in the surface reflectance.

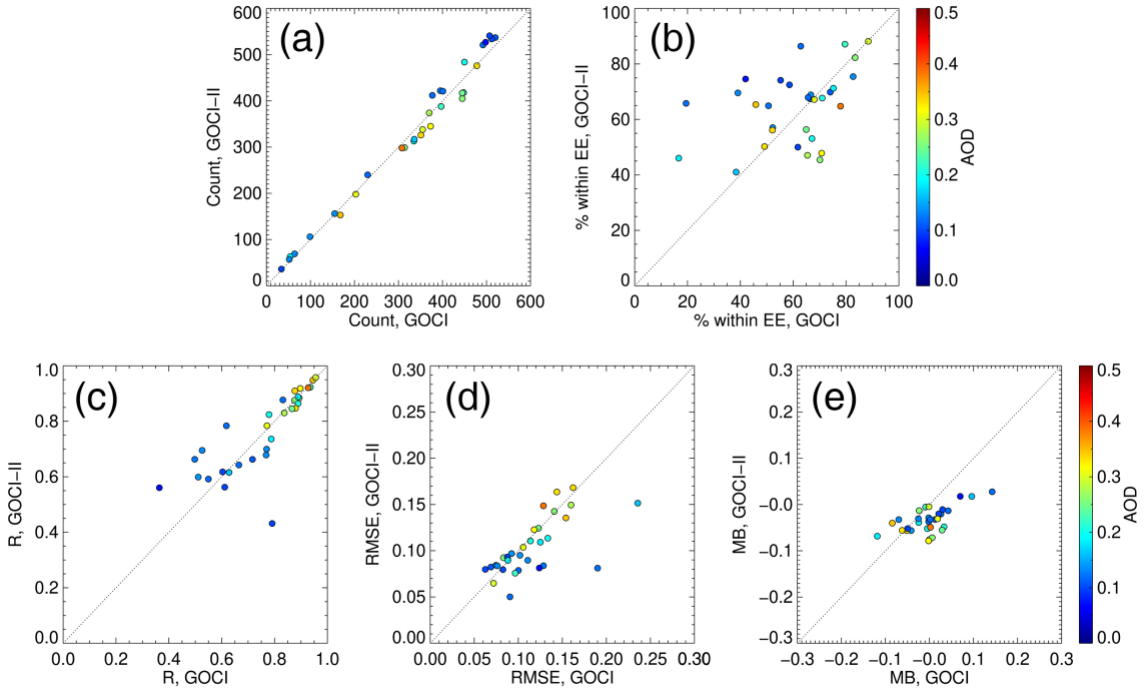

Figure 4. Comparison of site-by-site validation statistics between GOCI and GOCI-II AOD against AERONET: (a) number of co-located data available for the comparison, (b) the fraction of data points within the expected error, (c) correlation coefficient, (d) RMSE, and (e) median bias. The color of each point represents the average value of the AERONET AOD that is spatially and temporally collocated with the GOCI-II AOD. Black dotted lines represent one-to-one lines.

We performed an error analysis to investigate consistencies between the errors for the two satellite-derived datasets. Figure 5 shows the differences between the satellite-derived data and the AERONET AOD as a function of AERONET AOD, NDVI, scattering angle, and local observation time over land and ocean. In the analysis for AERONET AOD, NDVI, and scattering angle, each point represents the 50th percentile of 1,000 collocated data points,

sorted in ascending order for each x-axis value. For the local observation times, the number of data used in the analysis is also shown.

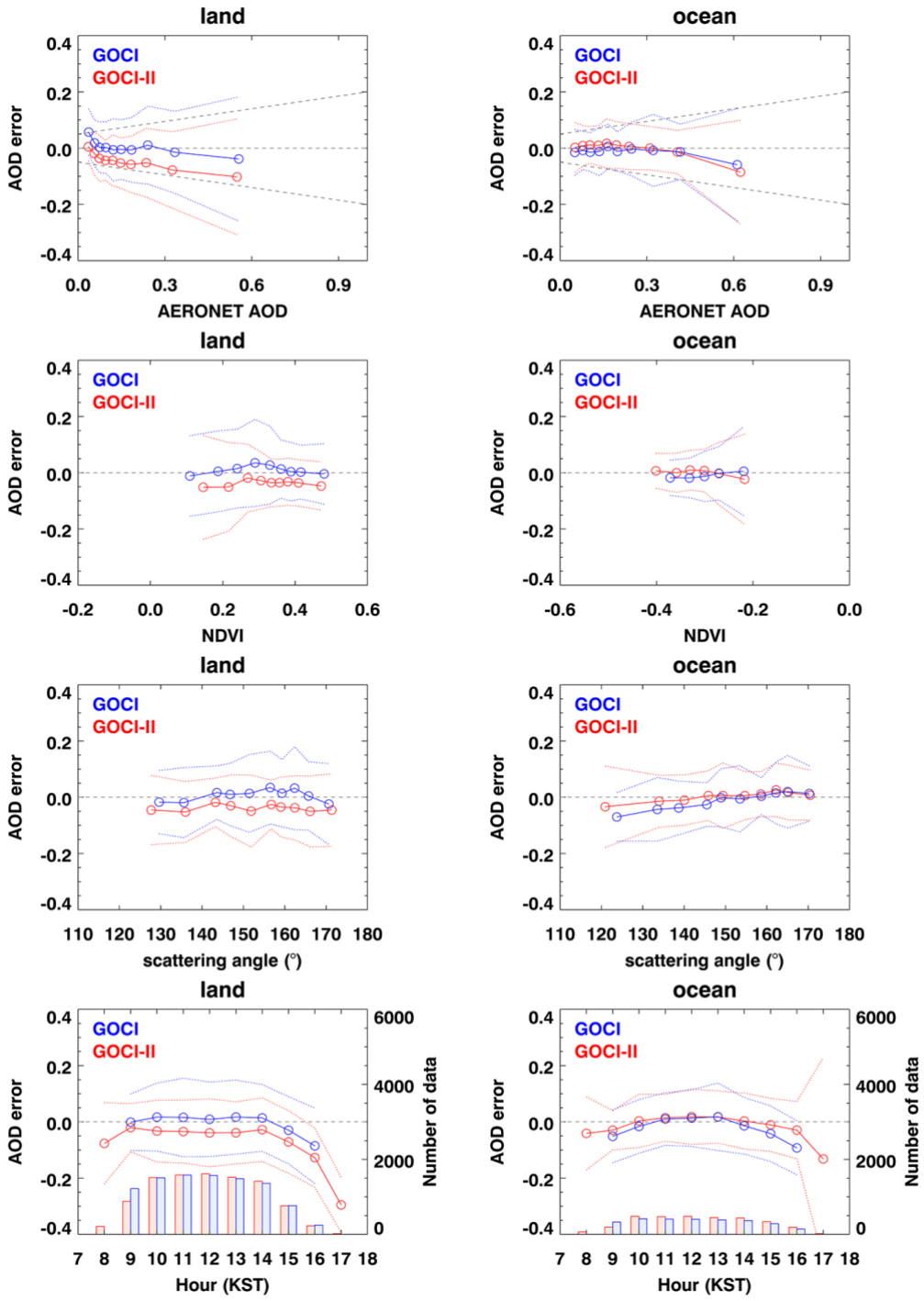

Figure 5. Differences between satellite-derived AOD and AERONET AOD as a function of AERONET AOD, NDVI, scattering angle, and local observation time (from top to bottom)

over land (left) and ocean (right). Each point and dotted line represent the median value and one standard deviation, respectively. GOCI results are shown in blue and GOCI-II results are shown in red.

GOCI-II AOD over land has a negative bias over all ranges of AERONET AOD, NDVI, and scattering angle, because of the overestimated surface reflectance. In contrast, GOCI AOD uses a climatological surface reflectance over land, leading to a lower bias. Despite these differences, the shapes of the AOD biases are the same for GOCI- and GOCI-II-retrievals. Unlike AOD over land, the biases for the GOCI and GOCI-II AODs over ocean have a similar magnitude. This is because Cox and Munk method was applied to estimate surface reflectance over open ocean, instead of the minimum reflectance method. The same error analysis was carried out for the results in Fig. S7, where the retrievals were based on two-year composite surface reflectance data. Compared with Fig. 5, the negative biases for the GOCI-II AOD over land are reduced in Fig. S7, but still remain. These differences might arise due to differences in the calibration of the two sensors or be influenced by variations in the retrieval algorithm, such as differences in radiative transfer model and aerosol model. Moreover, the presence of negative bias in the low AOD range indicates that it is still affected by background AOD. It can be reduced in future when long-term observation data are available from GOCI-II to estimate the surface reflectance.

There are more GOCI-II data than GOCI data for most observation times; however, this reverses at 9 KST, when there are more GOCI data. This is because slots from 7 to 11, which cover Eastern China and South Korea (Fig. S1), at 09 KST were not provided from December 21, 2020, to April 19, 2021, because of GOCI-II's wheel offloading.

3.2.2 Spatial and temporal consistency between the datasets

This section investigates various aspects of the consistency between the GOCI and GOCI-II AODs. Figure S8 shows the monthly averaged AODs at 550 nm for GOCI and GOCI-II from November 2020 to March 2021. We reproduced the daily AOD and then estimated the monthly mean AOD. No criteria for the number of data were applied for calculating daily mean AOD. To avoid contamination from snow-covered surfaces, the monthly average was calculated when AOD data were available for more than three days in the month, following the algorithm theoretical basis documents (ATBD) for the MODIS (Hubanks et al., 2015). Figure S8 demonstrates that the spatial coverage, which is affected by cloud, snow, and surface properties, was similar for the two satellite-derived AOD datasets. In most regions, the magnitude and spatial patterns for the GOCI and GOCI-II AODs are similar. However, some differences are noted. For example, the GOCI-II AOD is lower in eastern China than the GOCI AOD. As the background AOD is high in eastern China, this difference stems from an error in the estimated surface reflectance. This result is consistent with the result shown in Fig. 5(b).

For a comprehensive comparison of the spatial distribution of GOCI-II AOD with independent datasets, we utilized Aqua MODIS Collection 6.1 Level 3 DT and DB aerosol product as well as Suomi National Polar-orbiting Partnership (SNPP) VIIRS DB version 1.1 Level 3 aerosol product, which are provided on a 1° × 1° grid (Hsu et al., 2013; 2019; Levy et al., 2007; 2013; Sayer et al., 2017). All satellite datasets, including GOCI and GOCI-II, have similar AOD distributions, showing monthly variations of AOD with the highest values observed in March and AOD peaks in eastern China. Even though those data are averaged into coarse grids, AODs from MODIS and VIIRS show higher than those from GOCI and GOCI-II. This result might be caused by differences in aerosol retrieval algorithms including aerosol models and technique for estimating surface reflectance. Furthermore, the generation

of daily averaged AOD from hourly GOCI and GOCI-II observations might introduce smoothing of AOD values.

The spatial distribution of the statistics from the comparisons for the overlapping five months between GOCI and GOC-II AOD data are shown in Fig. 6. We compared hourly AOD data in 0.1° × 0.1° grids from GOCI and GOCI-II data. The correlation between the datasets is high in most regions (R = 0.8 or greater), particularly over the ocean. In regions where the correlation is low, such as in eastern China, AOD tends to be high, as shown in Fig. S8. For regions with weak correlations, the magnitudes of the RMSE and the median difference were also high. In particular, the GOCI-II AOD for eastern China in November and December was very low compared with the GOCI AOD for the same period and region. For some regions near the snow surface, the GOCI-II AOD is higher than the GOCI AOD. There could be snow affected pixels resulting AOD overestimation due to the absence of IR channels. When the AOD data are mapped to a 0.1° × 0.1° grid, there is a higher possibility of snow contamination for the GOCI-II data than for the GOCI data, as no criteria for the number of data were applied in the gridding process, and GOCI-II has higher spatial resolution than GOCI.

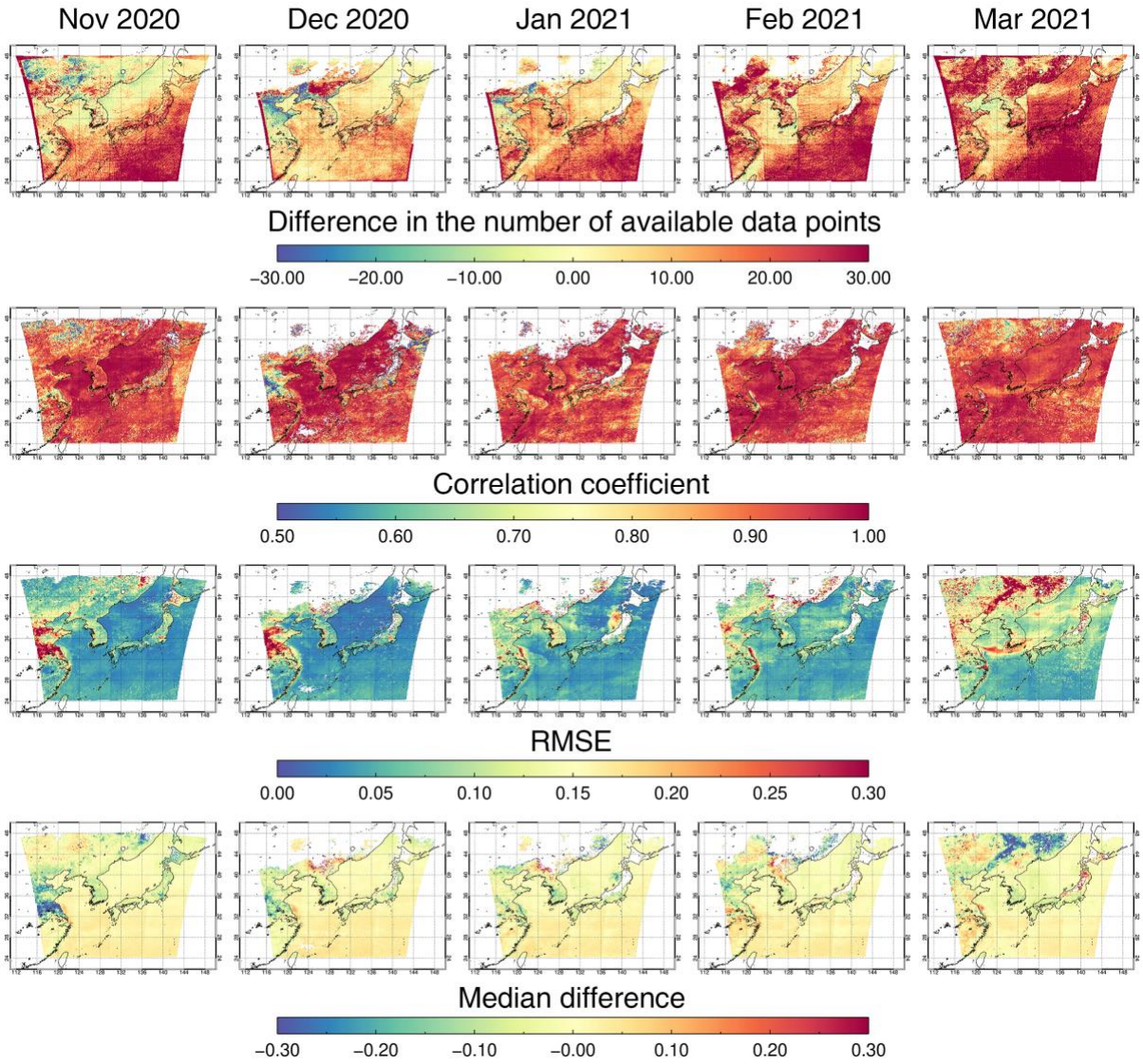

Figure 6. Statistics for comparisons between GOCI and GOCI-II retrievals of AOD from November 2020 to March 2021 (from left to right). From top to bottom, figures in each row show the difference in the number of available data points, the correlation, the RMSE, and the median difference (GOCI-II − GOCI).

We used the available GOCI and GOCI-II data to investigate AOD trends for major cities in East Asia in Fig. 7. The solid red line represents GOCI, the red dotted line represents GOCI-II, and yellow, blue, and green represent MODIS DT and DB products and the VIIRS DB product, respectively, which are calculated using monthly averaged datasets shown in Figs. S8

and S9. Figure 7 shows that all four satellite products have distinct seasonal variations, with high AOD from spring to early summer and low AOD in late fall. MODIS and VIIRS acquire images once or twice a day, whereas GOCI and GOCI-II acquire images several times a day. Thus, the AOD peak is higher in the MODIS products than in the GOCI- and GOCI-II-retrieved AODs, as the daily-averaging of the GOCI and GOCI-II AODs leads to smoothing of the peak. All the satellite datasets show a decline in AOD for major cities in East Asia from 2011 to 2021. GOCI-II shows a similar monthly variability to the other satellite products, including the period beyond the overlapping operation of GOCI and GOCI-II. This shows that a long-term aerosol record can be continuously accumulated for East Asia using GOCI and GOCI-II data. To achieve accurate long-term trend analysis in the future, efforts should be made to minimize the discrepancies between GOCI and GOCI-II AOD shown in section 3.2.1. Bias correction based on AERONET validation results or cross calibration of GOCI and GOCI-II TOA radiance can be employed to reduce the offset between two satellite datasets, facilitating more reliable long-term trend analysis.

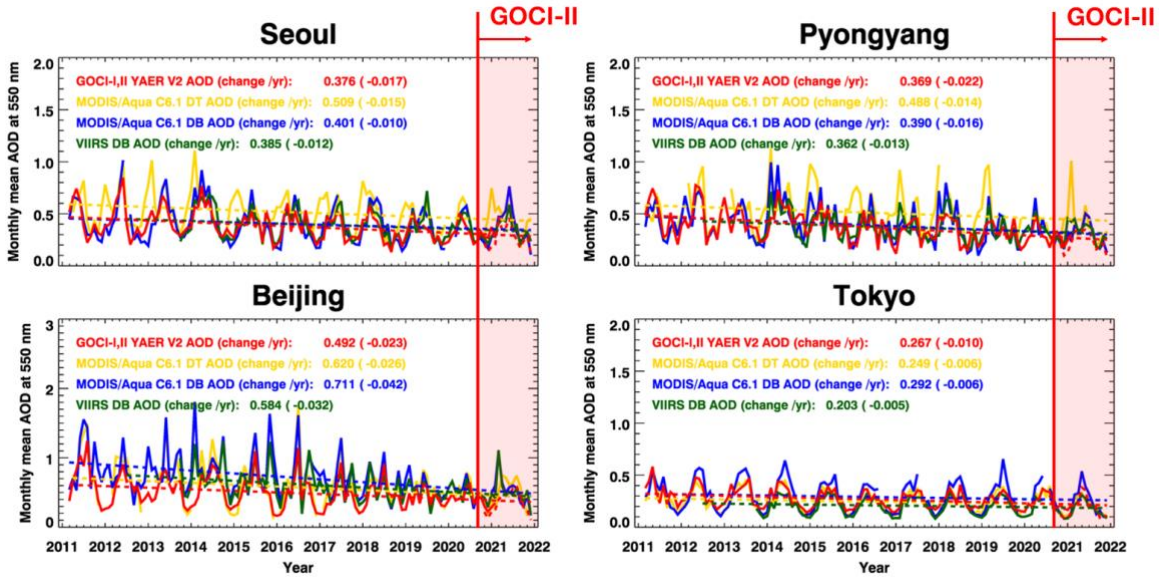

Figure 7. Time series of AOD at 550 nm from March 2011 to December 2021 for major cities

in East Asia. Red, yellow, blue, and green lines indicate monthly-averaged AODs retrieved from the GOCI, GOCI-II YAER, MODIS DT, MODIS DB, and VIIRS DB algorithms, respectively.

4. Summary and Conclusions

The purpose of this study was to retrieve aerosol optical properties from GOCI-II observation data. Furthermore, we evaluate whether GOCI-II data can be used to accurately retrieve hourly aerosol optical properties for East Asia to continue GOCI observations. In addition to calculating and evaluating the GOCI-II YAER product, we compared the accuracy and spatiotemporal characteristics of the GOCI and GOCI-II AODs to investigate consistency between the two satellite-derived aerosol products. We applied the YAER algorithm to GOCI-II data considering the improved performance of GOCI-II. Not only does the first AOD retrieval using GOCI-II shows good agreement with the GOCI AOD but also provides aerosol information at higher resolution than the GOCI data. The validation results for one year of GOCI-II AOD show that the product correlates with ground-based observation data with correlation coefficients of 0.824 and 0.794 over land and ocean, respectively. These results demonstrate that the YAER algorithm could be extended to other multi-channel satellite observations, as well as to GOCI and GOCI-II data.

The GOCI- and GOCI-II-retrieved AODs were compared for the period of their overlapping operation in several ways. Comparison with the AERONET AOD shows that both satellite-derived AODs have reliable accuracy, as measured using several statistical parameters. Slightly more data were available from GOCI-II for the comparison than from GOCI because of the high observation frequency of GOCI-II and the slight increase in the field of regard for GOCI-II relative to GOCI. The validation results were similar for the GOCI

and GOCI-II AODs, but there was a negative bias in the GOCI-II AOD over land due to its dependence on surface reflectance estimated from an insufficient period of data. The spatial coverage and distribution of GOCI and GOCI-II AODs are similar. Differences between the two AODs were associated with areas with high AOD. Our long-term time series analysis shows that the GOCI-II AOD results in similar AOD values to those calculated from other low-Earth-orbit satellite data, demonstrating that GOCI-II can provide aerosol data for East Asia to continue the record of GOCI.

All the findings in this study verify the successful extension of the YAER algorithm to GOCI-II data, and it is expected that the accuracy of GOCI-II aerosol products will improve further as long-term data are accumulated. Thus, continuous aerosol data in East Asia can be generated using the YAER algorithm to retrieve AOD from GOCI and GOCI-II observation data. Currently, the YAER algorithm has been applied to GOCI and GOCI-II, and also to data from the AHI to generate reliable aerosol data (Lim et al., 2018). In future, the algorithm could also be applied to other geostationary meteorological sensors, such as the AMI onboard the GK-2A platform and the Advanced Geostationary Radiation Imager (AGRI) onboard the Feng Yun-4A platform. As the specifications of next generation satellites improve in future, efforts to take advantage of more advanced data features will be required. For example, it may be possible to improve retrieval accuracy for SSA by exploiting the newly added ultraviolet region of GOCI-II observations. In addition, because GOCI-II is equipped with the Geostationary Environment Monitoring Spectrometer (GEMS) designed for observing air pollutants (Kim et al., 2020) onboard the same GK-2B platform, the synergy of two sensors will be also expected to perform accurate atmospheric correction. The improvement of the YAER algorithm and its application to data from state-of-the-art satellite technologies are expected to produce a long-term aerosol data record over East Asia and to be widely utilized in air quality and climate studies.

CRediT authorship contribution statement

Authors' individual contributions: Conceptualization SL JK MC; Data curation YJP JC JL MK; Investigation SL JK HL JL MK YC; Methodology SL JK MC HL; Resources YJP JC; Supervision JK; Writing – original draft SL; Writing – review & editing MC JK YJP; Funding acquisition JC.

Declaration of competing interest

The authors declare that they have no known competing financial interests or personal relationships that could have appeared to influence the work reported in this paper.

Acknowledgements

This research was supported by Korea Institute of Marine Science & Technology Promotion (KIMST) funded by the Ministry of Oceans and Fisheries (20220546). We acknowledge the free use of the MYD08M3, VIIRS DB and ERA5 datasets. The URL addresses where each of the data is available are stated in references below. Authors would like to acknowledge the support by the Korea Institute of Ocean Science and Technology (KIOST) for providing the GOCI and GOCI-II data. We also thank all the AERONET principal investigators and their staff for establishing and maintaining the AERONET sites used in this study.

References

Ahn, Y., Ryu, J., Cho, S., Kim, S., 2010. Missions and User Requirements of the 2nd Geostationary Ocean Color Imager (GOCI-II). Korean J. Remote Sens. 26, 277–285.

Choi, J., Park, Y.J., Ahn, J.H., Lim, H., Eom, J., Ryu, J., 2012. GOCI, the world's first geostationary ocean color observation satellite, for the monitoring of temporal variability in coastal water turbidity. J. Geophys. Res. 117, 1–10. https://doi.org/10.1029/2012JC008046

Choi, J.K., Park, M.S., Han, K.S., Kim, H.C., Im, J., 2021. One year of GOCI-II launch present and future. Korean J. Remote Sens. 37, 1229–1234. https://doi.org/10.7780/kjrs.2021.37.5.2.1

Choi, M., Kim, J., Lee, J., Kim, M., Park, Y., Holben, B., Thomas, F., Li, Z., Song, C.H., 2018. GOCI Yonsei aerosol retrieval version 2 aerosol products : improved algorithm description and error analysis with uncertainty estimation from 5-year validation over East Asia. Atmos. Meas. Tech. 11, 385–408.

Choi, M., Kim, J., Lee, J., Kim, M., Park, Y.J., Jeong, U., Kim, W., Hong, H., Holben, B., Eck, T.F., Song, C.H., Lim, J.H., Song, C.K., 2016. GOCI Yonsei Aerosol Retrieval (YAER) algorithm and validation during the DRAGON-NE Asia 2012 campaign. Atmos. Meas. Tech. 9, 1377–1398. https://doi.org/10.5194/amt-9-1377-2016

Copernicus Climate Change Service (C3S): ERA5: Fifth generation of ECMWF atmospheric reanalyses of the global cli- mate, Copernicus Climate Change Service Climate Data Store (CDS), available at: https://cds.climate.copernicus.eu/cdsapp#!/ home (last access: 27 December 2022), 2017.

Coste, P., Larnaudie, F., Luquet, P., Heo, H., Jung, J., Kang, G., Shin, S., Yong, S., Park, Y.-J., 2016. Development of the new generation of geostationary ocean color imager. Int. Conf. Sp. Opt. 10562, 105620D. https://doi.org/10.1117/12.2296099

Cox, C., Munk, W., 1954. Measurement of the Roughness of the Sea Surface from Photographs of the Sun's Glitter. J. Opt. Soc. Am. 44, 838.

https://doi.org/10.1364/josa.44.000838

Dubovik, O., King, M.D., 2000. A flexible inversion algorithm for retrieval of aerosol optical properties from Sun and sky radiance measurements. J. Geophys. Res. Atmos. 105, 20673–20696. https://doi.org/10.1029/2000JD900282

Eom, S., Kim, J., Lee, S., Holben, B.N., Eck, T.F., Park, S.-B., Park, S.S., 2022. Long-term variation of aerosol optical properties associated with aerosol types over East Asia using AERONET and satellite (VIIRS, OMI) data (2012–2019). Atmos. Res. 280, 106457. https://doi.org/10.1016/j.atmosres.2022.106457

Fukuda, S., Nakajima, T., Takenaka, H., Higurashi, A., Kikuchi, N., Nakajima, T.Y., Ishida, H., 2013. New approaches to removing cloud shadows and evaluating the 380 nm surface reflectance for improved aerosol optical thickness retrievals from the GOSAT/TANSO-Cloud and Aerosol Imager. J. Geophys. Res. 118, 13520–13531. https://doi.org/10.1002/2013JD020090

Giles, D.M., Sinyuk, A., Sorokin, M.G., Schafer, J.S., Smirnov, A., Slutsker, I., Eck, T.F., Holben, B.N., Lewis, J.R., Campbell, J.R., Welton, E.J., Korkin, S.V., Lyapustin, A.I., 2019. Advancements in the Aerosol Robotic Network (AERONET) Version 3 database – automated near-real-time quality control algorithm with improved cloud screening for Sun photometer aerosol optical depth (AOD) measurements. Atmos. Meas. Tech., 12, 169–209. https://doi.org/10.5194/amt-12-169-2019

Go, S., Kim, J., Mok, J., Irie, H., Yoon, J., Torres, O., Krotkov, N.A., Labow, G., Kim, M., Koo, J.-H., Choi, M., Lim, H., 2020. Ground-based retrievals of aerosol column absorption in the UV spectral region and their implications for GEMS measurements. Remote Sens. Environ. 111759. https://doi.org/10.1016/j.rse.2020.111759

Holben, B.N., Eck, T.F., Slutsker, I., Tanre, D., Buis, J.P., Setzer, A., Vermote, E., Reagan, J.A., Kaufman, Y.J., Nakajima, T., Lavenu, F., Jankowiak, I., Smirnov, A., 1998.

AERONET—A federated instrument network and data archive for aerosol characterization. Remote Sens. Environ., 66, 1–16.

Hsu, N.C., Jeong, M.J., Bettenhausen, C., Sayer, A.M., Hansell, R., Seftor, C.S., Huang, J., Tsay, S.C., 2013. Enhanced Deep Blue aerosol retrieval algorithm: The second generation. J. Geophys. Res. Atmos. 118, 9296–9315. https://doi.org/10.1002/jgrd.50712

Hsu, N.C., Lee, J., Sayer, A.M., Kim, W., Bettenhausen, C., Tsay, S.C., 2019. VIIRS Deep Blue Aerosol Products Over Land : Extending the EOS Long - Term Aerosol Data Records. J. Geophys. Res. Atmos. 124. https://doi.org/10.1029/2018JD029688

Hsu, N.C., Tsay, S.C., King, M.D., Herman, J.R., 2004. Aerosol properties over bright-reflecting source regions. IEEE Trans. Geosci. Remote Sens. 42, 557–569. https://doi.org/10.1109/TGRS.2004.824067

Hubanks, P.A., King, M.D., Platnick, S., Pincus, R., 2008. MOD 30-MODIS Atmosphere L3 Gridded Product. MODIS Atmos. L3 gridded Prod. Algorithm Theor. Basis Doc. ATBD-MOD-0, 96 pp.

Hyslop, N.P., 2009. Impaired visibility: the air pollution people see. Atmos. Environ. 43, 182–195. https://doi.org/10.1016/j.atmosenv.2008.09.067

Jin, S., Ma, Y., Huang, Z., Huang, J., Gong, W., Liu, B., Wang, W., Fan, R., Li, H., 2023. A comprehensive reappraisal of long-term aerosol characteristics, trends, and variability in Asia. Atmos. Chem. Phys., 23, 8187–8210, https://doi.org/10.5194/acp-23-8187-2023

Kang, Y., Kim, M., Kang, E., Cho, D., Im, J., 2022. Improved retrievals of aerosol optical depth and fine mode fraction from GOCI geostationary satellite data using machine learning over East Asia. ISPRS J. Photogramm. Remote Sens. 183, 253-268. https://doi.org/10.1016/j.isprsjprs.2021.11.016

Kim, J., Jeong, U., Ahn, M.H., Kim, J.H., Park, R.J., Lee, Hanlim, Song, C.H., Choi, Y.S., Lee, K.H., Yoo, J.M., Jeong, M.J., Park, S.K., Lee, K.M., Song, C.K., Kim, Sang Woo, Kim, Y.J.,

636 Kim, Si Wan, Kim, M., Go, S., Liu, X., Chance, K., Miller, C.C., Al-Saadi, J., Veihelmann,
637 B., Bhartia, P.K., Torres, O., Abad, G.G., Haffner, D.P., Ko, D.H., Lee, S.H., Woo, J.H.,
638 Chong, H., Park, S.S., Nicks, D., Choi, W.J., Moon, K.J., Cho, A., Yoon, J., Kim, S. kyun,
639 Hong, H., Lee, K., Lee, Hana, Lee, S., Choi, M., Veefkind, P., Levelt, P.F., Edwards, D.P.,
640 Kang, M., Eo, M., Bak, J., Baek, K., Kwon, H.A., Yang, J., Park, J., Han, K.M., Kim, B.R.,
641 Shin, H.W., Choi, H., Lee, E., Chong, J., Cha, Y., Koo, J.H., Irie, H., Hayashida, S., Kasai,
642 Y., Kanaya, Y., Liu, C., Lin, J., Crawford, J.H., Carmichael, G.R., Newchurch, M.J., Lefer,
643 B.L., Herman, J.R., Swap, R.J., Lau, A.K.H., Kurosu, T.P., Jaross, G., Ahlers, B., Dobber,
644 M., McElroy, C.T., Choi, Y., 2020. New era of air quality monitoring from space:
645 Geostationary environment monitoring spectrometer (GEMS). Bull. Am. Meteorol. Soc.
646 101, E1–E22. https://doi.org/10.1175/BAMS-D-18-0013.1
647 Koo, J.H., Kim, Jhoon, Lee, Y.G., Park, S.S., Lee, S., Chong, H., Cho, Y., Kim, Jaemin, Choi,
648 K., Lee, T., 2020. The implication of the air quality pattern in South Korea after the
649 COVID-19 outbreak. Sci. Rep. 10, 1–11. https://doi.org/10.1038/s41598-020-80429-4
650 Lee, J., Hsu, N.C., Sayer, A.M., Seftor, C.J., Kim, W. V., 2021. Aerosol Layer Height with
651 Enhanced Spectral Coverage Achieved by Synergy between VIIRS and OMPS-NM
652 Measurements. IEEE Geosci. Remote Sens. Lett. 18, 949–953.
653 https://doi.org/10.1109/LGRS.2020.2992099
654 Lee, J., Kim, J., Song, C.H., Kim, S.B., Chun, Y., Sohn, B.J., Holben, B.N., 2010a.
655 Characteristics of aerosol types from AERONET sunphotometer measurements. Atmos.
656 Environ. 44, 3110–3117. https://doi.org/10.1016/j.atmosenv.2010.05.035
657 Lee, J., Kim, J., Song, C.H., Ryu, J.H., Ahn, Y.H., Song, C.K., 2010b. Algorithm for retrieval
658 of aerosol optical properties over the ocean from the Geostationary Ocean Color Imager.
659 Remote Sens. Environ. 114, 1077–1088. https://doi.org/10.1016/j.rse.2009.12.021
660 Lee, S., Kim, Jhoon, Choi, M., Hong, J., Lim, H., Eck, T.F., Holben, B.N., Ahn, J.Y., Kim,

Jeongsoo, Koo, J.H., 2019. Analysis of long-range transboundary transport (LRTT) effect on Korean aerosol pollution during the KORUS-AQ campaign. Atmos. Environ. 204, 53–67. https://doi.org/10.1016/j.atmosenv.2019.02.020

Lee, S., Kim, M., Kim, S.Y., Lee, D.W., Lee, H., Kim, J., Le, S., Liu, Y., 2020. Assessment of long-range transboundary aerosols in Seoul, South Korea from Geostationary Ocean Color Imager (GOCI) and ground-based observations. Environ. Pollut. in press, 115924. https://doi.org/10.1016/j.envpol.2020.115924

Levy, R.C., Mattoo, S., Munchak, L.A., Remer, L., Sayer, A.M., Patadia, F., Hsu, N.C., 2013. The Collection 6 MODIS aerosol products over land and ocean. Atmos. Meas. Tech. 6, 2989–3034. https://doi.org/10.5194/amt-6-2989-2013

Levy, R.C., Munchak, L.A., Mattoo, S., Patadia, F., Remer, L.A., Holz, R.E., 2015. Towards a long-term global aerosol optical depth record: Applying a consistent aerosol retrieval algorithm to MODIS and VIIRS-observed reflectance. Atmos. Meas. Tech. 8, 4083–4110. https://doi.org/10.5194/amt-8-4083-2015

Levy, R.C., Remer, L.A., Mattoo, S., Vermote, E.F., Kaufman, Y.J., 2007. Second-generation operational algorithm: Retrieval of aerosol properties over land from inversion of Moderate Resolution Imaging Spectroradiometer spectral reflectance. J. Geophys. Res. Atmos. 112, 1–21. https://doi.org/10.1029/2006JD007811

Li, J., Carlson, B.E., Yung, Y.L., Lv, D., Hansen, J., Penner, J.E., Liao, H., Ramaswamy, V., Kahn, R.A., Zhang, P., Dubovik, O., Ding, A., Lacis, A.A., Zhang, L., Dong, Y., 2022. Scattering and absorbing aerosols in the climate system. Nat. Rev. Earth Environ. 3, 363–379. https://doi.org/10.1038/s43017-022-00296-7

Lim, H., Choi, M., Kim, J., Kasai, Y., Chan, P.W., 2018. AHI/Himawari-8 Yonsei aerosol retrieval (YAER): Algorithm, validation and merged products. Remote Sens. 10. https://doi.org/10.3390/rs10050699

686 Park, M.E., Song, C.H., Park, R.S., Lee, J., Kim, J., Lee, S., Woo, J.H., Carmichael, G.R., Eck,
687 T.F., Holben, B.N., Lee, S.S., Song, C.K., Hong, Y.D., 2014. New approach to monitor
688 transboundary particulate pollution over Northeast Asia. Atmos. Chem. Phys. 14, 659–674.
689 https://doi.org/10.5194/acp-14-659-2014
690 Pendergrass, D.C., Zhai, S., Kim, J., Koo, J.H., Lee, S., Bae, M., Kim, S., Liao, H., Jacob,
691 D.J., 2022. Continuous mapping of fine particulate matter (PM2.5) air quality in East Asia
692 at daily 6×6km^2 resolution by application of a random forest algorithm to 2011 2019 GOCI
693 geostationary satellite data. Atmos. Meas. Tech. 15, 1075–1091.
694 https://doi.org/10.5194/amt-15-1075-2022
695 Saleh, R., Robinson, E.S., Tkacik, D.S., Ahern, A.T., Liu, S., Aiken, A.C., Sullivan, R.C,
696 Presto, A.A., Dubey, M.K., Yokelson, R.J., Donahue, N.M., Robinson, A.L., 2014.
697 Brownness of organics in aerosols from biomass burning linked to their black carbon
698 content. Nat. Geosci. 7, 647–650. https://doi.org/10.1038/ngeo2220
699 Sawyer, V., Levy, R.C., Matto, S., Cureton, G., Shi, Y., Remer, L.A., 2020. Continuing the
700 MODIS Dark Target Aerosol Time Series with VIIRS. Remote Sens. 12, 308.
701 https://doi.org/10.3390/rs12020308
702 Sayer, A.M., Hsu, N.C., Lee, J., Bettenhausen, C., Kim, W. V., Smirnov, A., 2018. Satellite
703 Ocean Aerosol Retrieval (SOAR) Algorithm Extension to S-NPP VIIRS as Part of the
704 “Deep Blue” Aerosol Project. J. Geophys. Res. Atmos. 123, 380–400.
705 https://doi.org/10.1002/2017JD027412
706 Sayer, A.M., Hsu, N.C., Lee, J., Kim, W. V., Dutcher, S.T., 2019. Validation, stability, and
707 consistency of MODIS Collection 6.1 and VIIRS Version 1 Deep Blue aerosol data over
708 land. J. Geophys. Res. Atmos. https://doi.org/10.1029/2018jd029598
709 Spurr, R.J.D., 2006. VLIDORT: A linearized pseudo-spherical vector discrete ordinate
710 radiative transfer code for forward model and retrieval studies in multilayer multiple

711 scattering media. J. Quant. Spectrosc. Radiat. Transf. 102, 316–342. https://doi.org/
712 10.1016/j.jqsrt.2006.05.005.
713 Spurr, R., Christi, M., 2019. The LIDORT and VLIDORT linearized scalar and vector discrete
714 ordinate radiative transfer models: Updates in the last 10 years. In: Kokhanovsky, A. (Ed.),
715 Springer Series in Light Scattering: Volume 3: Radiative Transfer and Light Scattering.
716 Springer International Publishing, Cham, pp. 1–62. https://doi.org/10.1007/978-3-030-
717 03445-0_1.
718 Yong, S.-S., Kang, G.-S., Huh, S., Cha, S.-Y., 2021. Current Status and Results of In-orbit
719 Function, Radiometric Calibration and INR of GOCI-II (Geostationary Ocean Color
720 Imager 2) on Geo-KOMPSAT-2B. Korean J. Remote Sens. 37, 1235–1243.
721 Zhai, S., Jacob, D.J., Brewer, J.F., Li, K., Moch, J.M., Kim, J., Lee, S., Lim, H., Lee, H.C.,
722 Kuk, S.K., Park, R.J., Jeong, J.I., Wang, X., Liu, P., Luo, G., Yu, F., Meng, J., Martin, R. V.,
723 Travis, K.R., Hair, J.W., Anderson, B.E., Dibb, J.E., Jimenez, J.L., Campuzano-Jost, P.,
724 Nault, B.A., Woo, J.H., Kim, Y., Zhang, Q., Liao, H., 2021. Relating geostationary satellite
725 measurements of aerosol optical depth (AOD) over East Asia to fine particulate matter
726 (PM2.5): insights from the KORUS-AQ aircraft campaign and GEOS-Chem model
727 simulations. Atmos. Chem. Phys. 21, 16775–16791. https://doi.org/10.5194/acp-21-16775-
728 2021
729 Zhang, Y., Li, Z., Zhang, Y., Hou, W., Xu, H., Chen, C., Ma, Y., 2014. High temporal
730 resolution aerosol retrieval using Geostationary Ocean Color Imager: application and initial
731 validation. J. Appl. Remote Sens. 8, 083612. https://doi.org/10.1117/1.JRS.8.083612
732